communications earth & environment

A Nature Portfolio journal

Article

https://doi.org/10.1038/s43247-025-02437-4

Offshore wave and wind energy development in the Southern Hemisphere will remain optimal between 20°E and 180°E by 2100

Check for updates

Xiaohu Zhao[1,2], Guohe Huang[3,4] ✉, Yongping Li[2], Chen Lu[5], Chuyin Tian[6], Tangnyu Song[7], Xiong Zhou[2], Wenchang Tang[2] & Bo Pang[2]

Wave and offshore-wind energies offer promising alternatives to fossil fuels, yet their combined potential under climate change remains poorly understood. Here we assess how climate change may affect this potential over the coming century, using outputs from fifteen global climate models included in the Coupled Model Intercomparison Project Phase 6 and an empirical method to refine model projections. We identify two oceanic bands between 40°S and 60°S with high combined energy potential. Notably, the region between 20°E and 180°E is projected to remain favorable for both energy sources. We also conduct a multi-level analysis to show how improved climate modeling enhances predictions of renewable energy resources. These findings provide valuable insights for policymakers, industry stakeholders, and researchers seeking to enhance the resilience and sustainability of renewable energy systems.

The pressing imperative to transition from fossil fuels to renewable energy sources stems from escalating concerns about climate change. Among various renewable energy alternatives, wave and offshore-wind energies have received significant attention due to their immense untapped potentials[1–3]. The combined utilization of wave and offshore-wind energies offers the opportunity to increase the overall efficiency and reliability of renewable energy systems[4,5]. Moreover, it has the potential to reduce operating costs and optimize power generation[6]. However, the impacts of climate change on atmospheric and oceanic dynamics can alter wind patterns and wave characteristics, and thus the spatiotemporal availability and accessibility of wave and offshore-wind energy resources[1,7,8]. A comprehensive understanding of such impacts is essential for the effective planning, design, and operation of offshore renewable energy systems. It can also serve as a cornerstone for informing policy decisions aimed at achieving a sustainable and resilient energy transition.

The previous studies[9–11] were focused on combined potentials of wave and offshore-wind energies for individual regions and/or historical periods. Most existing studies focus on nearshore regions or areas with immediate technical and economic feasibility, often neglecting the broader spatial context and long-term resource availability. However, to inform comprehensive renewable energy planning, it is crucial to explore energy resources beyond current limitations. There was a scarcity of research on such potential for multiple regions or relevant projections for the future. Moreover, multiple climate models and emission scenarios were considered in the previous studies[12–14]; they were mostly based on conventional sensitivity analyses. However, there was no report in investigating the significance of the variations among the simulated potentials of wave and offshore-wind energies under multiple emission and climate-model scenarios and, more importantly their interrelated settings.

Therefore, to address the above challenges, the objective of this study is to comprehensively evaluate the combined potentials of wave and offshore-wind energies at a global scale in the upcoming century under changing climatic conditions. This study extends the analysis beyond the constraints of current technical and economic feasibility to capture the complete spatial

[1]School of Geoscience and Technology, Zhengzhou University, Zhengzhou, China. [2]State Key Joint Laboratory of Environmental Simulation and Pollution Control, School of Environment, Beijing Normal University, Beijing, China. [3]State Key Joint Laboratory of Environmental Simulation and Pollution Control, China-Canada Center for Energy, Environment and Ecology Research, UR-BNU, School of Environment, Beijing Normal University, Beijing, China. [4]Environmental Systems Engineering Program, University of Regina, Regina, Canada. [5]The Abdus Salam International Centre for Theoretical Physics, Trieste, Italy. [6]Department of Geography & Environmental Management, University of Waterloo, Ontario, Canada. [7]School of Marine and Atmospheric Science, Stony Brook University, Stony Brook, USA. ✉e-mail: huang@iseis.org

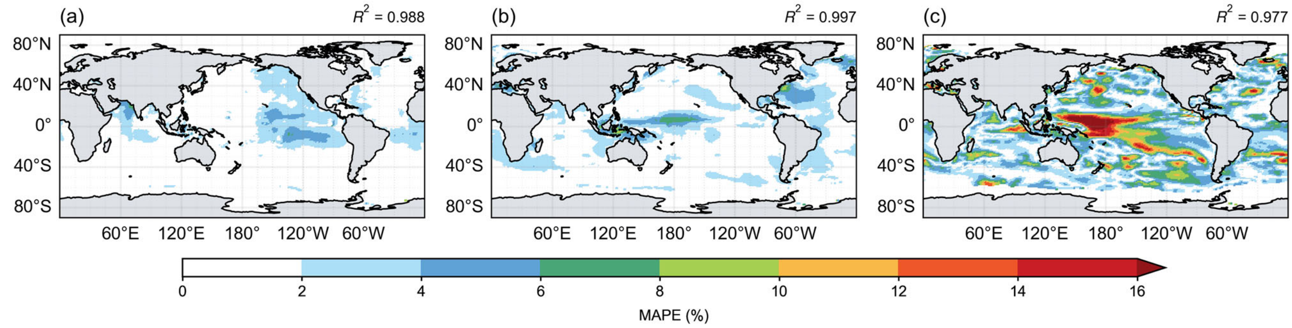

Fig. 1 | Spatial validation of the downscaled climate model ensemble. The maps show the spatial distribution of mean absolute percentage error (MAPE) for the validation period (2005–2014). The MAPE is calculated by comparing the Bayesian Model Averaging (BMA) ensemble of downscaled CMIP6 model outputs against the ERA5 reference data. The error distributions are shown for: **a** Peak wave period (pp1d); **b** Significant height of combined wind waves and swell (swh); and **c** 100 m wind speed (ws100).

distribution and long-term availability of combined wave and offshore-wind energy resources. This will be accomplished based on the integrated consideration of multiple climate models and emission scenarios and their interrelationships through multi-level factorial analysis. This study encompasses the following components: (a) ensemble simulation of the potentials for global wave and offshore-wind energies for the periods of 2031–2060 and 2071–2100, based on fifteen Coupled Model Intercomparison Project Phase 6 (CMIP6) models under three climate-change scenarios (i.e., SSP1-2.6, SSP2-4.5, and SSP5-8.5), (b) assessment of combined potentials of wave and offshore-wind energies in the upcoming century under three climate-change scenarios, based on the ensemble-simulation results, and (c) analysis for the variations of the simulated potentials of wave and offshore-wind energies under multiple emission and climate-model scenarios and their interrelated settings through the development of a multi-level factorial analysis approach.

Results

Evaluation of modeling performance

Before investigating the renewable energy potential, the performance of the developed empirical Bayesian ensemble downscaling model should be evaluated. The general goal for climate projections is to maximize the projected accuracy and reliability. The coefficient of determination (R^2) and mean absolute percentage error (MAPE) are used in this study to evaluate the accuracy of deterministic projections. These metrics are calculated based on downscaled outputs and ERA5 reference data for 2005–2014. The individual empirically downscaled CMIP6 global climate model (GCM) outputs, which form the input ensemble for the Bayesian model averaging (BMA), already demonstrate considerable skill. For example, for peak wave period (pp1d), these model outputs exhibit a MAPE below 2% across 68% of areas, with an R^2 exceeding 0.977 (Supplementary Fig. 1). Notably, the EC-Earth3-Veg-LR model demonstrates MAPE < 2% over 77% of areas (Supplementary Fig. 1i). Similarly, for significant height of combined wind waves and swell (swh), all models produce MAPE < 2% over 56% of areas, with R^2 greater than 0.993 (Supplementary Fig. 2). For 100 m wind speed (ws100), the downscaled results from all models exhibit MAPE < 6% across more than 66% of areas, and R^2 exceeding 0.962 (Supplementary Fig. 3). The subsequent application of BMA to this multi-model ensemble further enhances predictive skill and provides robust probabilistic projections (Fig. 1). The BMA ensemble exhibits high accuracy, particularly for wave climate parameters. Specifically, the R^2 for pp1d and swh are 0.988 and 0.997, respectively. The corresponding domain-averaged MAPE values are 1.26% for pp1d and 1.68% for swh, with MAPE remaining below 2% across the majority (>70%) of areas for both variables (Fig. 1a, b). For ws100, the BMA ensemble achieves an average MAPE of 4.55%, with values below 6% in over 75% of areas, although higher errors (>10%) are noted in specific regions, such as from the equator to the South Pacific (Fig. 1c).

To demonstrate the reliability of the model, the coverage, interval width, and ratio of coverage and interval width are evaluated for several confidence levels (10%, 20%, 40%, 75% and 95%) (Fig. 2). The coverages for pp1d, swh, and ws100 at the 40% confidence interval are greater than 80%. For the ensemble projection of swh, the coverage is greater than 60% at the 10% confidence interval. Comparing the ratio of coverage and interval width for swh and ws100, the ensemble projection of swh has twice the coverage of ws100 at the same narrow confidence interval (10%). These indicate that the developed model is reliable for pp1d, swh, and ws100 projections, especially for swh.

Historical high wave and offshore-wind energy potentials and their combined potentials

A high energy potential location is defined as having energy surpassing the 90th percentile of global energy potential during the corresponding period. Understanding the spatial distribution of regions with both high wave and offshore-wind energy potentials is crucial for optimizing resource utilization and making informed decisions. Notably, our study uniquely emphasizes mid-ocean areas, which, while demonstrating high theoretical energy potential, face significant practical constraints under current conditions. By adopting an optimistic outlook on future technological progress, we aim to provide a comprehensive assessment of these regions, thereby highlighting their long-term strategic importance for renewable energy planning. Additionally, characterizing the specific features of wave and offshore-wind energy potentials within these regions under climate change can provide valuable insights for promoting these energy sources as viable and sustainable alternatives.

Figure 3 depicts the spatial distribution of regions with high wave energy potential, offshore-wind energy potential, and locations suitable for their combined development during the baseline period (1985–2014). During the baseline period, the region with high wave energy potential predominantly spans from latitudes 40°S to 60°S and longitudes 10°E to 70°W (Fig. 3a). Notably, areas where wave energy potential exceeds 95 kW/m predominantly occur in the southern Indian Ocean. Furthermore, the areas characterized by high offshore-wind energy potential align latitudinally with regions of high wave energy potential and span across the Western Hemisphere. In contrast to wave energy, the central Indian Ocean, western Arabian Sea, central Pacific Ocean, and Caribbean Sea all exhibit high offshore-wind energy potential (Fig. 3b). Regions with high offshore-wind energy potential are predominantly situated in the southern Indian Ocean and southeast Atlantic Ocean, while regions with high wave energy potential are mainly located in the southern Indian Ocean and Pacific Ocean. The regions characterized by both high offshore-wind and wave energy potentials are situated along two distinct bands between latitudes 40°S and 60°S (Fig. 3c). The presence of high wave and offshore-wind energy potentials at high latitudes in the Southern Hemisphere, particularly within the latitudinal bands of 40°S to 60°S, is strongly influenced by the Southern

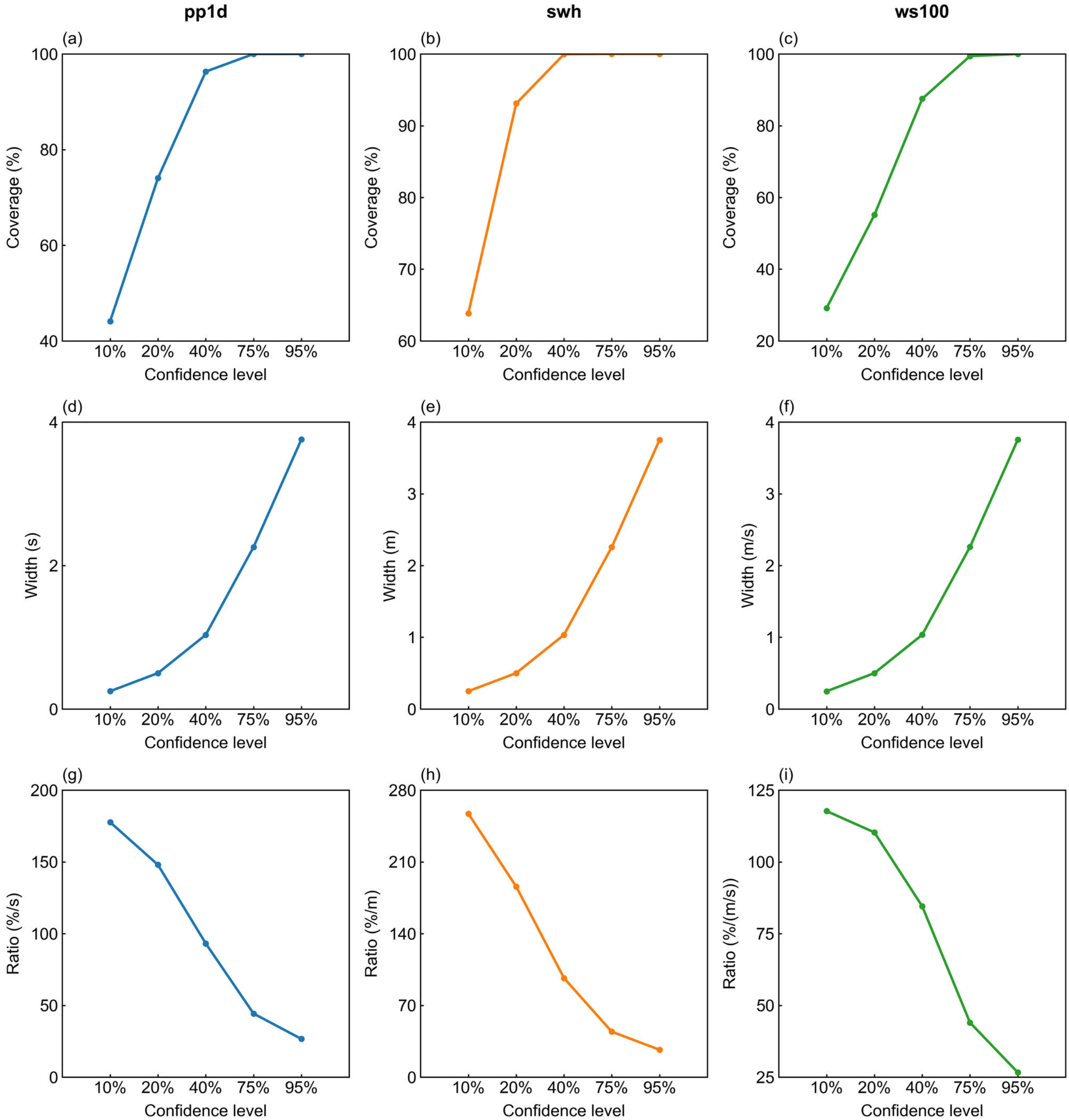

Fig. 2 | Reliability assessment of the developed empirical Bayesian ensemble downscaling model. The figure evaluates the model's reliability in simulating peak wave period (pp1d), significant height of combined wind waves and swell (swh), and 100 m wind speed (ws100). **a**–**c** Coverage at 10%, 20%, 40%, 75%, and 95% confidence intervals for pp1d (**a**), swh (**b**), and ws100 (**c**). **d**–**f** Interval width at corresponding confidence levels for pp1d (**d**), swh (**e**), and ws100 (**f**). **g**–**i** Ratio of coverage to interval width for pp1d (**g**), swh (**h**), and ws100 (**i**).

Hemisphere Annular Mode (SAM), also known as the Antarctic Oscillation[15]. The SAM, characterized as a large-scale pattern of atmospheric variability in the Southern Hemisphere, plays a significant role in the weather and climate patterns of the high and middle latitudes in the Southern Hemisphere[16]. This influence extends to the wave energy potential and offshore-wind energy potential.

Future changes in high wave and offshore-wind energy potentials

The future high offshore renewable energy potential is assessed during two periods (2031–2060, 2071–2100) under three climate change scenarios (SSP1-2.6, SSP2-4.5, and SSP5-8.5). The future spatial distribution of high wave energy potential closely resembles that of the baseline period, with a concentration in the latitudinal bands of 40°S to 60°S and within the Indian and Pacific Oceans (Fig. 4). Across different future periods and scenarios, it is projected that areas with wave energy potential exceeding 95 kW/m will experience varying degrees of decrease compared to the baseline period. Specifically, during 2071–2100 under SSP5-8.5, the decrease is anticipated to exceed 50% (Fig. 4f). The wave energy potential in the region between 120°W and 160°W is expected to increase in the future and exceed 95 kW/m. Furthermore, the area of this region is

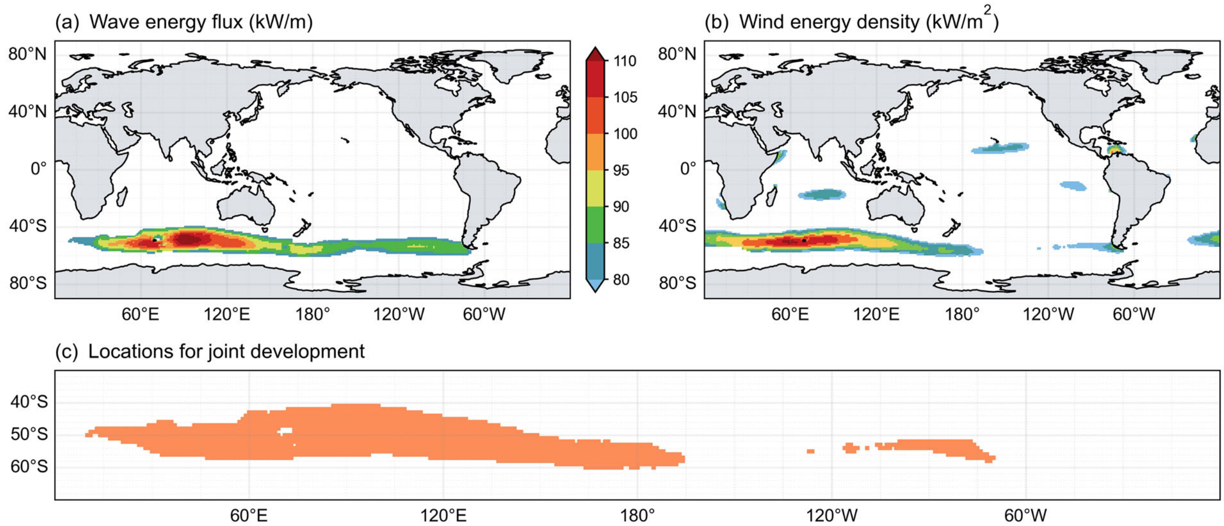

Fig. 3 | Spatial distribution of high wave and offshore-wind energy potentials during the baseline period (1985–2014). a Regions with high wave energy potential. **b** Regions with high offshore-wind energy potential. **c** Locations with potential for combined wave and offshore-wind energy development.

projected to be larger during 2071–2100 compared to 2031–2060, with a greater increase in area at a higher greenhouse gas emission scenario. For instance, under SSP5-8.5, the area expansion is projected to reach 40.42% during 2071–2100. Unlike wave energy potential, the spatial layout of future high offshore-wind energy potential will change compared to the baseline period, with changes towards a more elongated latitudinal distribution (Fig. 5). Compared to the baseline period, during 2031–2060, the two bands of high offshore-wind energy potential between 40°S and 60°S are projected to extend eastward and westward, respectively, with a tendency to form a continuous and complete band (Fig. 5a, c, e). By 2071–2100, under SSP5-8.5, these two bands will be connected to form a nearly complete band of high offshore-wind energy potential (Fig. 5b, d, f). The future high offshore-wind energy area in the central Indian Ocean is projected to progressively decrease compared to the baseline period, and it may even cease to exist entirely under SSP5-8.5 by 2071–2100 (Fig. 5f). The offshore-wind energy potential in the waters south of Hawaii is anticipated to experience an increase in both area and magnitude, surpassing the levels observed during the baseline period. Specifically, the area with high offshore-wind energy potential is expected to expand by 77.13 % under SSP5-8.5 during 2071–2100. Concurrently, the region's offshore-wind energy potential is projected to rise by up to 40.67 %.

Deterministic and probabilistic projections of locations for combined development of wave and offshore-wind energy

The deterministic and probabilistic projections of locations for combined development of wave and offshore-wind energy during two future periods (i.e., 2031–2060 and 2071–2100) under three climate change scenarios (i.e., SSP1-2.6, SSP2-4.5, and SSP5-8.5) are obtained from BMA approach. The overlap region in Fig. 6 provides valuable insight into the areas where the BMA deterministic and probabilistic projections exhibit a consensus, indicating locations with favorable conditions for harnessing significant energy from both wave and offshore-wind resources. This consensus suggests a high level of confidence in the potential for combined development of wave and offshore-wind energy in these areas. Furthermore, the observed distribution of these consensus areas between 20°E and 180°E signifies that the agreement between the BMA deterministic and probabilistic forecasts is prevalent across this longitudinal range. This widespread consensus supports the notion that the identified regions within this range offer promising opportunities for the simultaneous utilization of wave and offshore-wind energy resources. The variations observed in the cyan, blue, and red areas highlight the divergence between the deterministic and probabilistic projections, enabling a comprehensive understanding of the uncertainties associated with forecasting future sites for high wave and offshore-wind energies. The divergence between the BMA deterministic and probabilistic predictions for future high wave energy and offshore-wind energy regions is primarily observed in the longitude ranges of 0 to 20°E, 0 to 10°W, and along the edges of the consensus region. The BMA deterministic projection effectively captures the essential characteristics of the spatial distributions, providing a representation of the anticipated locations for combined development of wave and offshore-wind energy in the future. The convergence of two prominent regions featuring high wave energy and offshore-wind energy potentials is projected to occur in the future, particularly during 2071–2100, under high emission scenarios such as SSP5-8.5 (Fig. 6f).

To analyze the characteristics of the probability density function (PDF) for high wave energy and offshore-wind energy under changing climate conditions, the kernel density estimation method[17] is implemented. This approach enables the estimation of the PDF, providing insights into the distribution of these energy variables. The future high wave energy potential exhibits an increased probability of falling below 85 kW/m when compared to the baseline period (Fig. 7a, c). The probability of falling below 85 kW/m is more significant under higher concentration emission scenarios, such as under SSP5-8.5 for 2071–2100, with an increase of up to 26.27% compared to the baseline period (Fig. 7c). In contrast, the probability of wave energy potential exceeding 90 kW/m is projected to decline in future periods, with reductions exceeding 7.16%. Additionally, mean high wave energy potential is expected to decrease by 1.21 kW/m, 1.53 kW/m, and 2.07 kW/m (1.66 kW/m, 2.95 kW/m, and 4.98 kW/m) during 2031 – 2060 (2071 – 2100) under SSP1-2.6, SSP2-4.5, and SSP5-8.5, respectively. The probability of high offshore-wind energy potential in the range of 0.4–0.6 kW/m^2 is expected to increase during 2031–2060 compared to the baseline period, with a maximum increase of 4.42%. The probability of high offshore-wind energy potential exceeding 0.45 kW/m^2 is projected to increase during 2071–2100 (Fig. 7d). In contrast to high wave energy potential, the mean high offshore-wind energy potential is projected to increase in future periods. Specifically, this increase is estimated at approximately 0.03 kW/m^2 under SSP1-2.6, 0.06 kW/m^2 under SSP2-4.5, and 0.09 kW/m^2 under SSP5-8.5 during 2071 – 2100. The probability of wave energy potential exceeding 90 kW/m within the combined development areas is expected to decrease in the coming

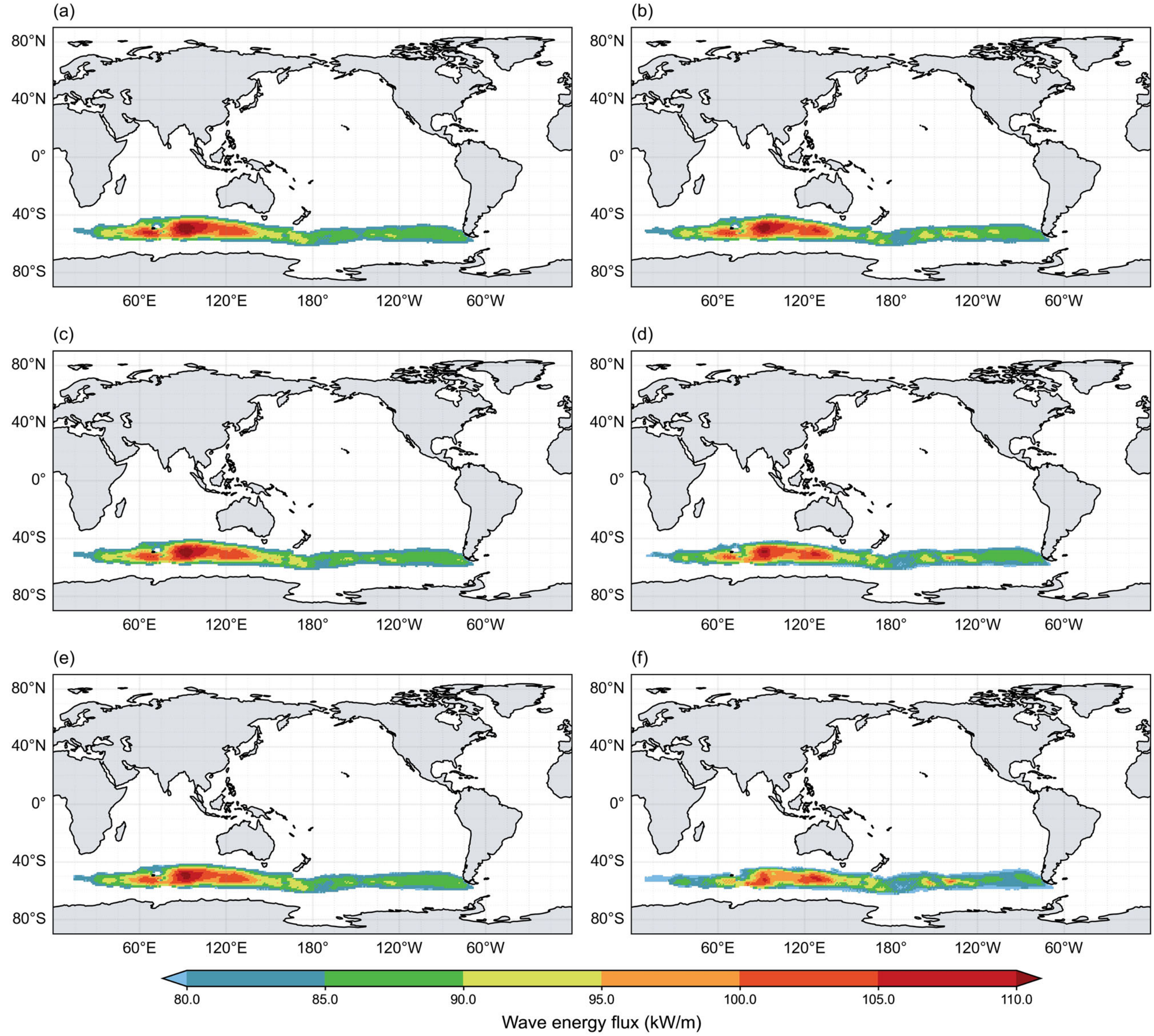

Fig. 4 | Spatial distribution of regions with high wave energy potential under future climate scenarios. a, b Projections under SSP1-2.6 for 2031–2060 (**a**) and 2071–2100 (**b**). **c**, **d** Projections under SSP2-4.5 for 2031–2060 (**c**) and 2071–2100 (**d**). **e**, **f** Projections under SSP5-8.5 for 2031–2060 (**e**) and 2071–2100 (**f**).

periods, with a maximum reduction of up to 27.99% (Fig. 8a, c). The probability of future offshore-wind energy potential in these areas at both low and high values will increase (Fig. 8b, d). Specifically, under SSP5-8.5, the probability of offshore-wind energy potential exceeding 0.7 kW/m^2 will increase during 2071–2100, with a rise of 19.00% (Fig. 8d).

Multi-level factorial analysis of the uncertainty sources in wave and offshore-wind energy potential projections

Multi-level factorial analysis is used to investigate the uncertainties associated with projected wave and offshore-wind energy potentials, considering variations in different climate models and climate change scenarios. Figure 9 presents the spatial distribution of the dominant contributing factor, boxplots of the contributing factors and the statistical significance of climate models for wave and offshore-wind energy potentials. Climate models are identified as the dominant source of uncertainty for both wave and offshore-wind energy potentials in most of the world (Fig. 9a, b). Climate change scenarios dominate the uncertainty in the projected wave energy potential in areas within the southern Indian Ocean, northern Pacific Ocean, and North Atlantic (Fig. 9a). For the offshore-wind energy potential projections, climate change scenarios dominate the uncertainty in areas within the south-central Indian Ocean, the western Pacific, and the western North Atlantic (Fig. 9b). For wave energy potential projections, the spatial mean contributions explained by climate models, climate change scenarios, and the interrelated settings of climate models and climate change scenarios are 70.13%, 5.98%, and 4.60%, respectively (Fig. 9c). Similarly, for offshore-wind energy potential, the spatial mean contributions of climate models, climate change scenarios, and the interrelated settings of climate models and climate change scenarios are 70.47%, 5.84%, and 5.10%, respectively (Fig. 9d). Notably, the spatial mean contribution of inter-decadal variation, treated as an error term in this study, to wave and offshore-wind energy potentials is 19.28% and 18.59%, respectively. It underscores the considerable impact that inter-decadal variation has on both wave and offshore-wind energy potentials. Climate models play a significant role in projecting wave and offshore-wind energy potentials in nearly every grid cell (Fig. 9e, f).

Conclusions

Transitioning to a low-carbon or even zero-carbon energy system is a key strategy for mitigating global warming that relies on the expansion of renewable energy. Wave and offshore-wind energies are promising

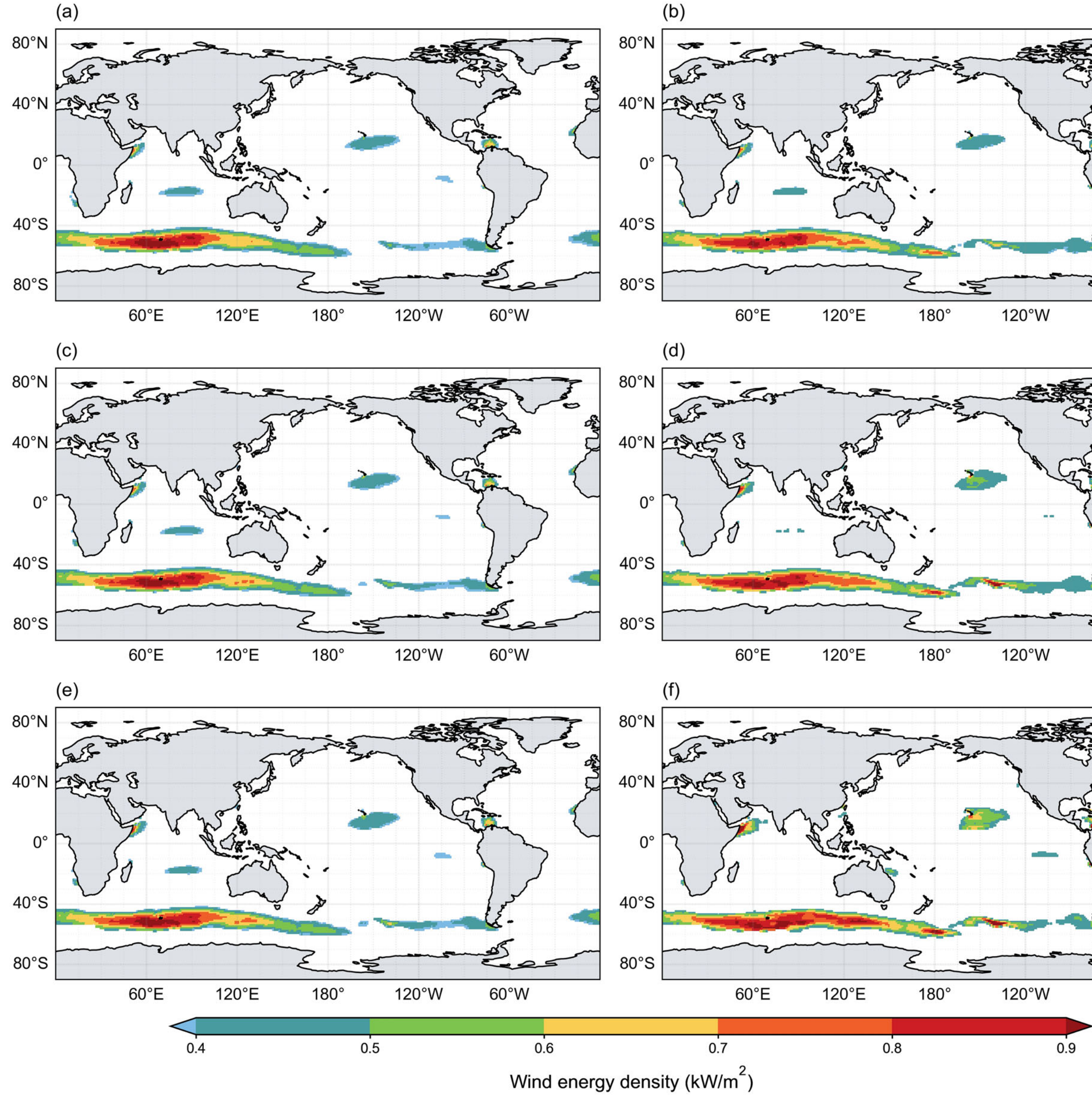

Fig. 5 | Spatial distribution of regions with high offshore-wind energy potential under future climate scenarios. **a**, **b** Projections under SSP1-2.6 for 2031–2060 (**a**) and 2071–2100 (**b**). **c**, **d** Projections under SSP2-4.5 for 2031–2060 (**c**) and 2071–2100 (**d**). **e**, **f** Projections under SSP5-8.5 for 2031–2060 (**e**) and 2071–2100 (**f**).

renewable energy sources, but their vulnerability to climate dynamics remains a critical issue. There is a notable lack of comprehensive and detailed assessments of the impact of global climate change on these energy sources. Our analysis therefore extends beyond conventional regional studies to evaluate global-scale variability and long-term potential of wave and offshore-wind resources under future climate scenarios. To address this knowledge gap, we employ an empirical Bayesian ensemble downscaling method using data from fifteen sets of CMIP6 GCMs and the ERA5 reanalysis to investigate the characteristics of wave and offshore-wind energy potentials under three climate change scenarios. The spatial distribution of high wave energy potential is projected to remain consistent with the baseline period, concentrated between latitudes 40°S and 60°S, particularly in the southern Indian Ocean and Pacific Ocean. However, there is a projected decrease in areas with wave energy potential greater than 95 kW/m, especially under SSP5-8.5 during 2071–2100. On the other hand, the offshore-wind energy potential shows a spatial shift characterized by an expansion of the latitudinal distribution and the formation of continuous high potential zones between 40°S and 60°S. In addition, certain regions, such as the central Indian Ocean, may experience a gradual decrease in offshore-wind energy potential. The BMA approach provides deterministic and probabilistic projections for the combined development of wave and offshore-wind energy, highlighting consensus areas where both resources can be harnessed effectively. These consensus regions offer promising opportunities for the simultaneous utilization of wave and offshore-wind energy resources, particularly between 20°E and 180°E. Projected average wave energy potential declines, whereas average offshore-wind energy potential is expected to increase, particularly under SSP5-8.5 during 2071–2100. It should be noted that regions with high offshore-wind energy potential often coincide with harsh weather conditions, which may challenge the structural resilience and long-term operation of offshore energy devices, and while offshore-wind energy is currently more efficient and commercially viable, wave energy systems can provide complementary benefits, for example by mitigating wave-induced loads on floating wind turbines, thereby underscoring the potential of integrated hybrid systems under future energy scenarios. Multi-level factorial analysis shows that climate models are the primary source of uncertainty in wave and offshore-wind energy potential projections, underscoring the importance of advancing climate modeling. These findings contribute to a comprehensive

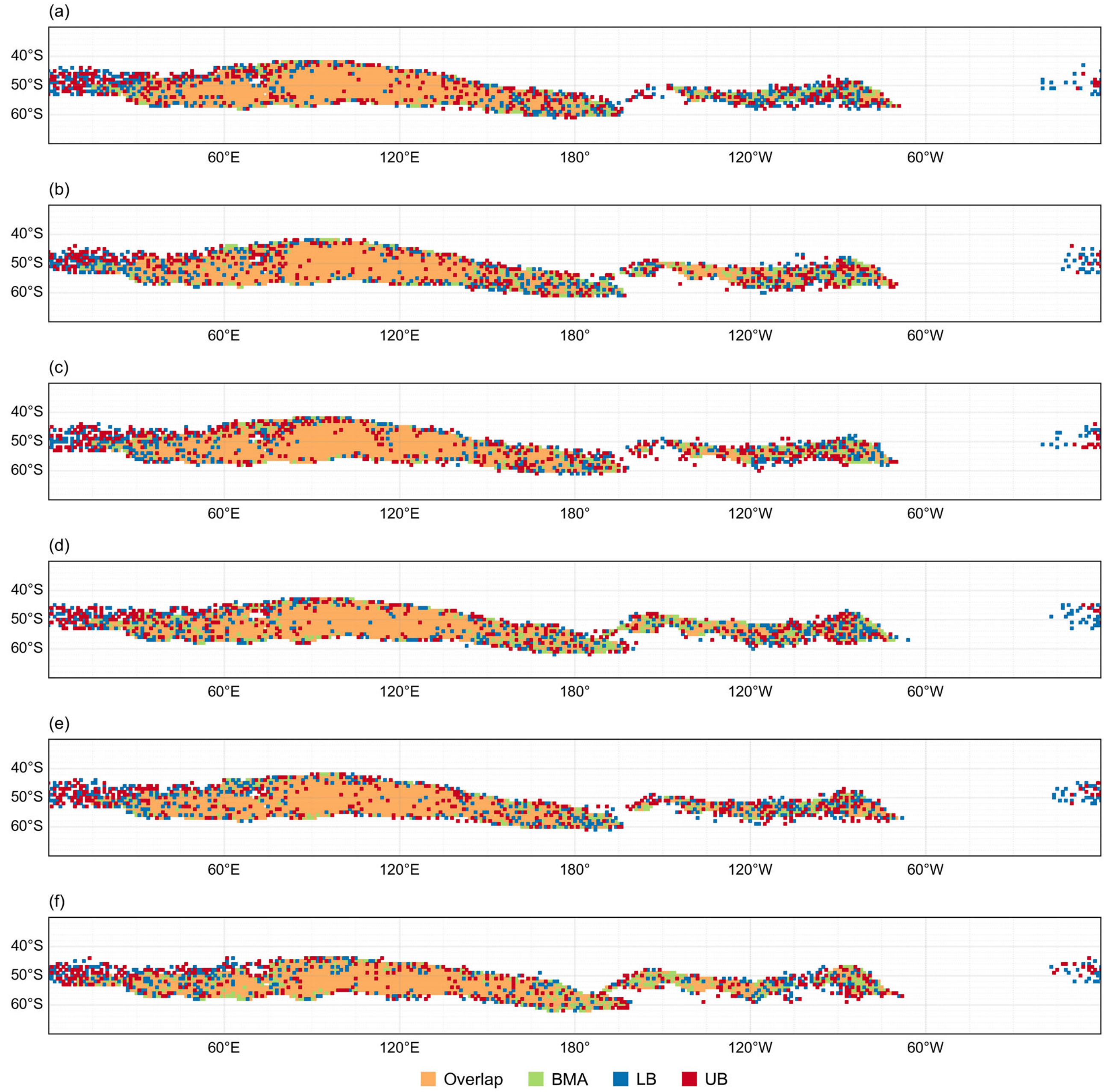

Fig. 6 | BMA deterministic and probabilistic projections of locations suitable for combined development of wave and offshore-wind energy under future climate scenarios. a, c, e Projections for the period 2031–2060 under SSP1-2.6, SSP2-4.5, and SSP5-8.5, respectively. **b, d, f** Projections for the period 2071–2100 under SSP1-2.6, SSP2-4.5, and SSP5-8.5, respectively. Cyan indicates the BMA deterministic projection; blue and red denote the lower bound (LB) and upper bound (UB) of the BMA 95% projection interval, respectively; orange indicates the overlap of deterministic and probabilistic projections.

assessment of the wave and offshore-wind energies, enabling stakeholders to make informed choices and develop effective strategies to harness and manage these renewable energy resources in a changing climate.

Methods

Data

Large-scale atmospheric variables from fifteen CMIP6[18] climate models including surface upward sensible heat flux (hfss), sea level pressure (psl), surface downwelling shortwave radiation (rsds), near-surface wind speed (sfcWind), near-surface air temperature (tas), eastward near-surface wind (uas), northward near-surface wind (vas), sea surface temperature (tos), water flux into ocean (wfo), sea surface height above geoid (zos), are used as predictors for the empirical downscaling model in this study. Three shared socioeconomic pathways (i.e., SSP1-2.6, SSP2-4.5, and SSP5-8.5) are considered in this study. Monthly outputs of 100 m wind speed (ws100, calculated from 100m u- and v-components of wind), significant height of combined wind waves and swell (swh), and peak wave period (pp1d) are retrieved from the latest generation ECMWF reanalysis dataset (ERA5)[19]. ERA5 is proven to be one of the reliable global reanalysis products by previous studies and is widely used as a reference dataset to improve the accuracy and reliability of climate model simulations. The CMIP6 model outputs are empirically downscaled and ensembled using ERA5 outputs to generate reliable wave and offshore-wind simulations. Both CMIP6 and ERA5 reanalysis outputs are bilinearly re-gridded to $1° \times 1°$ grids to match the spatial resolution. The empirical downscaling and Bayesian ensemble model are trained and calibrated in the training period (1985–2004). The models trained in

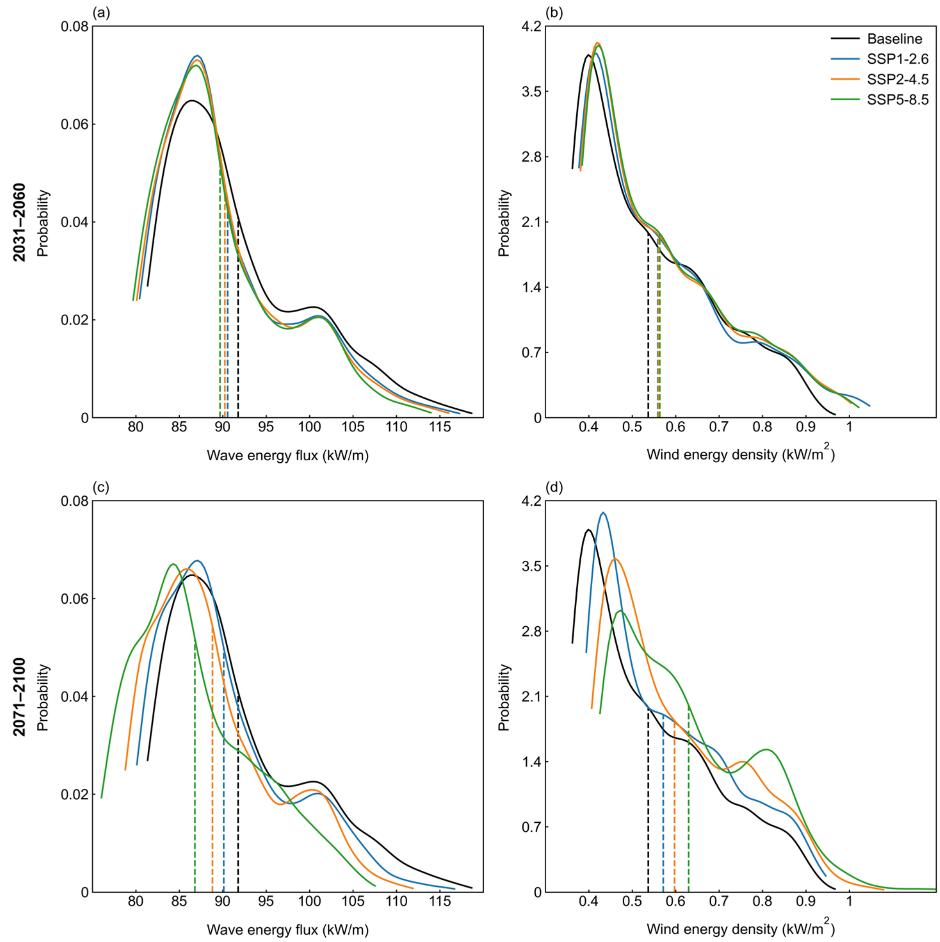

Fig. 7 | Probability density functions (PDFs) of regions with high wave and offshore-wind energy potentials. a, c Wave energy potential during 2031–2060 and 2071–2100, respectively. **b, d** Offshore-wind energy potential during 2031–2060 and 2071–2100, respectively.

each grid are then evaluated in the validation period (2005–2014). Offshore renewable energy potential in the baseline period (1985–2014) and two future periods (2031–2060, 2071–2100) are assessed in this study. Detailed information on the climate models and reanalysis used in this study is provided in Supplementary Table 1.

Bayesian ensemble of empirical downscaling climate model outputs

High uncertainty stems in atmospheric variable simulations of global climate models (GCMs)[20,21]. To generate robust model projections, empirical downscaling and Bayesian ensemble approaches are used in this study, using ERA5 reanalysis as reference. The linear regression is applied to empirically downscale the CMIP6 model simulations. The empirical downscaling models can be expressed by the following form.

$$Y_{downscaled} = ED(X_{hfss}, X_{psl}, X_{rsds}, X_{sfcWind}, X_{tas}, X_{uas}, X_{vas}, X_{tos}, X_{wfo}, X_{zos}) \tag{1}$$

where $Y_{downscaled}$ denotes the predictands, $X_{...}$ represents the large-scale atmospheric predictors from the raw CMIP6 outputs. $ED(\cdot)$ denotes the empirical downscaling model.

Different climate models may advance in different aspects of climate processes or patterns, while no individual climate model or combination of climate models can be superior to others under all conditions. Reliable climate ensemble projections are needed for adaption or mitigation actions to global warming. Bayesian model averaging (BMA)[22,23] is widely used to generate reliable probabilistic ensemble projections by competing several climate model projections. BMA ascertain consensus projections by weighted averaging individual model projections based on their posterior probabilities[24]. The statistical inference scheme of BMA is assigning higher weights to better performing model simulations than the worse acting ones. The weights can reflect the relative contributions of models to simulation skill. The Bayesian probabilistic ensemble projection of a climate variable y can be represented by the following expression.

$$p(y|f, R) = \sum_{i=1}^{N} p(f_i|R) p_i(y|f_i, R) \tag{2}$$

where $p(y|f, R)$ denotes the probability density function of y given the individual model output (f_i) and reference dataset (R), $p(f_i|R)$ indicates the posterior probability of model output (f_i) referring the correct projection given the reference dataset (R), and $p_i(y|f_i, R)$ denotes the posterior distribution of y given the individual model output (f_i) and reference dataset (R). The posterior model probability $p(f_i|R)$ is known as weights, so that $\sum_{i=1}^{N} p(f_i|R) = \sum_{i=1}^{N} w_i = 1$.

The posterior mean and variance of BMA projection can be expressed as:

$$E[y|O, f] = \sum_{m=1}^{M} p(f_i|R) \cdot E[p_i(y|f_i, R)] = \sum_{i=1}^{N} w_i f_i \tag{3}$$

$$Var[y|R, f] = \sum_{i=1}^{N} w_i \left(f_i - \sum_{i=1}^{N} w_i f_i \right)^2 + \sum_{i=1}^{N} w_i \sigma_i^2 \tag{4}$$

Fig. 8 | Probability density functions (PDFs) of high wave and offshore-wind energy potentials in locations identified for combined development. a, c Wave energy potential during 2031–2060 and 2071–2100, respectively. **b, d** Offshore-wind energy potential during 2031–2060 and 2071–2100, respectively.

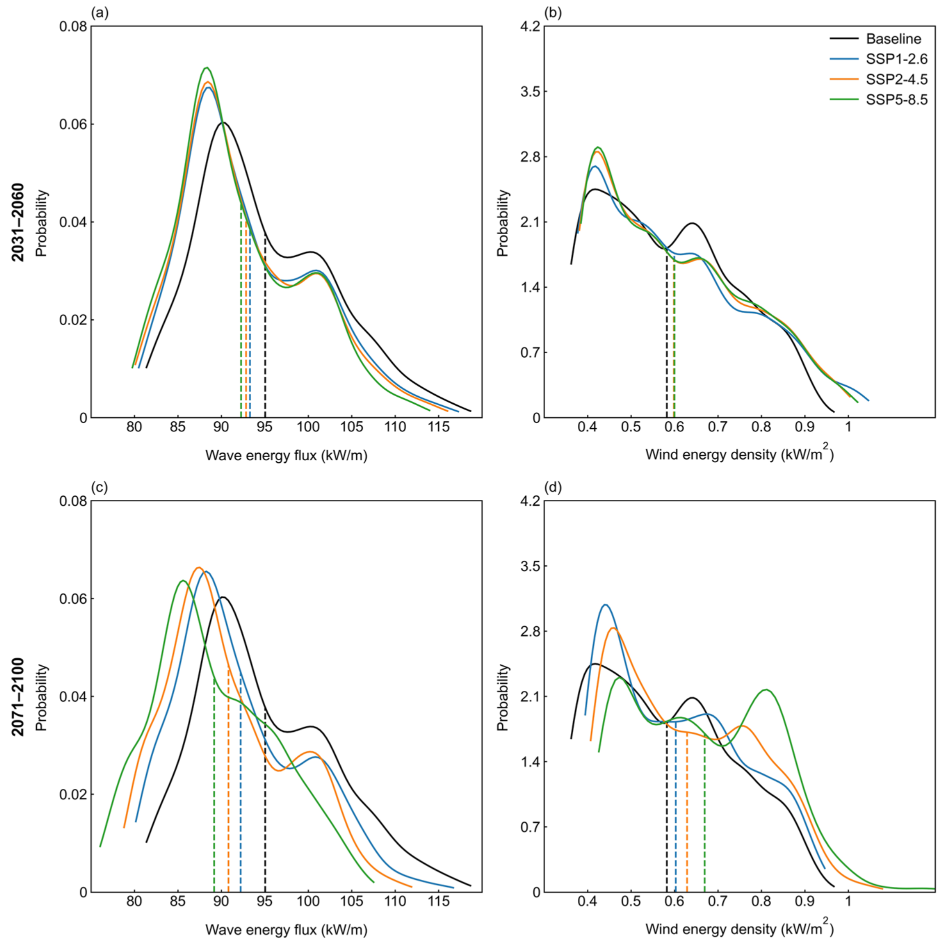

where σ_i^2 is the expected variance related to the individual model output (f_i) conditioned on reference dataset (R). The BMA variance can be decomposed into two components: the between-model and the within-model variance. The non-BMA ensemble approach can only consider the between-model variance, consequently generating under-dispersive projection.

The BMA approach assumes that the conditional probability distribution $p_i(y|f_i, R)$ is Gaussian. Box-Cox transformation method[25] is used to transform both the model projections and reference data close to the Gaussian distribution. The parameter set ($\theta = \{w_i, \sigma_i, i = 1, 2, \ldots, N\}$) can be estimated through maximizing the log-likelihood function:

$$l(\theta) = \log\left[\sum_{i=1}^{N} w_i \cdot p_i(y|f_i, R)\right] \tag{5}$$

The expectation-maximization (EM) algorithm[26] is used in this study to obtain the analytical solution of the parameter set. The probabilistic ensemble projections can be derived by competing individual model projections:

Step 1: Generate a value of i from the number set {1, ..., N} based on the probability set $\{w_1, \ldots, w_N\}$.

Step 2: Generate a value of y_j from the conditional probability density function $p_i(y|f_{i,j}, R)$.

Step 3: Repeat Steps (1) and (2) K times. The K is set to be 100 in this study.

Step 4: Set $j = j + 1$. If j reaches M, stop; else go to Step (1).

Coverage and interval width are fundamental metrics in evaluating BMA ensemble simulations for climate forecasting. Coverage measures the reliability by assessing how often observed values fall within the predicted intervals, while interval width indicates the precision of the forecasts, with narrower intervals being preferable for decision-making.

Calculation of wave and offshore-wind energy potentials

Wave energy potential can be estimated through the wave energy flux (P_{wave}, kW/m)[27,28].

$$P_{wave} = \frac{1}{64\pi}\rho_{water} g^2 H_s^2 T_p \tag{6}$$

where ρ_{water} is the water density, which can be assumed to be a constant value of 1023.6 kg/m^3 at standard sea water conditions[29]; g indicates the gravitational acceleration (9.81 m/s^2 in this study); H_s denotes the significant wave height; T_p is the peak wave period.

Wind energy density (P_{wind}, kW/m^2) is a widely used measure of offshore-wind energy potential, which is defined as:

$$P_{wind} = \frac{1}{2}\rho_{air} V_{wind} \tag{7}$$

where ρ_{air} indicates the air density, which is typically assumed to be a constant value of 1.213 kg/m^3 at standard climate conditions[30]; V_{wind} denotes the offshore-wind speed at the 100 m hub height.

High energy potential is defined using a threshold-based approach in this study. A location of high energy potential is identified as location which the energy potential is above the 90th percentile of the global energy potential over the corresponding period. Location for combined development (L_{CD}) is a location with both high wave (L_{wave}) and offshore-wind (L_{wind}) energy

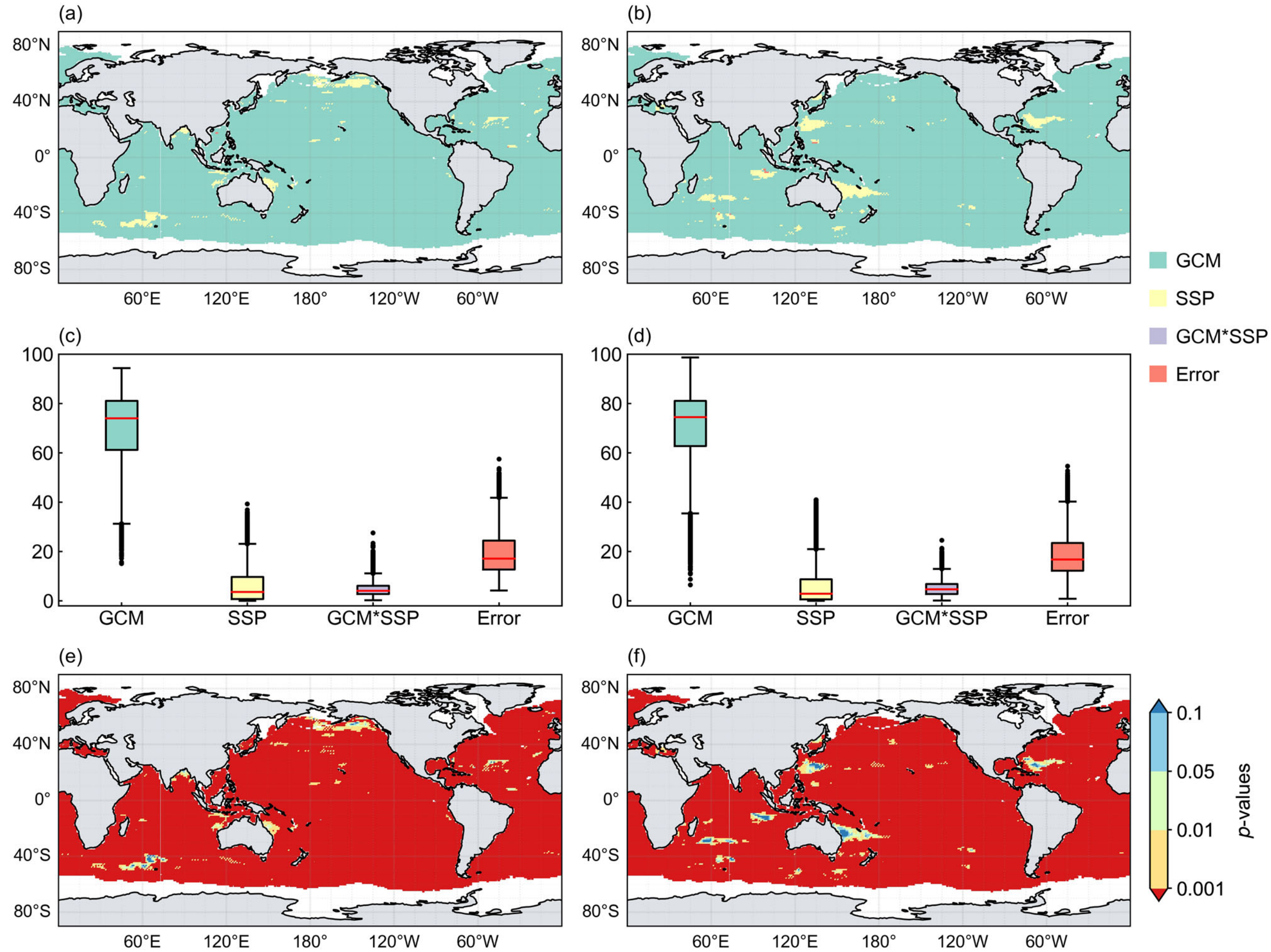

Fig. 9 | Analysis of contributing factors and climate model significance for wave and offshore-wind energy potentials. a, b Spatial distribution of dominant contributing factors. **c, d** Boxplots of contributing factor values: center red line (median), box (IQR, 25th–75th percentiles), whiskers (1.5×IQR), gray points (outliers). **e, f** Statistical significance of climate models. Columns correspond to wave energy (left) and offshore-wind energy (right), respectively.

potentials.

$$L_{CD} = L_{wave} \cap L_{wind} \tag{8}$$

Multi-level factorial analysis

Due to uncertainties in climate model structure and/or climate change, the climate projections produced by multiple climate models can be distinctly different. Multiple GCM-SSP combinations can produce different offshore renewable energy potential projections, with disparities especially pronounced at regional scales. Thus, the multi-level factorial analysis approach is developed to characterize associated uncertainties in the offshore renewable energy potential projections. The uncertainty sources of CMIP6 models (GCM) and climate change scenarios (SSP), as well as their interrelated settings (GCM × SSP), are investigated through multi-level factorial analysis at each grid. The factorial design information is presented in Supplementary Table 2. The total variability of the projections can be partitioned into the following components[31]:

$$SS_{total} = \sum_{i}^{a}\sum_{j}^{b}\sum_{k}^{c} y_{ijk}^{2} - \frac{y_{...}^{2}}{abc};\, y_{...} = \sum_{i}^{a}\sum_{j}^{b}\sum_{k}^{c} y_{ijk} \tag{9}$$

$$SS_{A} = \frac{1}{bc}\sum_{i}^{a} y_{i..}^{2} - \frac{1}{abc} y_{...}^{2};\, y_{i..} = \sum_{j}^{b}\sum_{k}^{c} y_{ijk}\; i = 1, 2, \ldots, a \tag{10}$$

$$SS_{B} = \frac{1}{ac}\sum_{j}^{b} y_{.j.}^{2} - \frac{1}{abc} y_{...}^{2};\, y_{.j.} = \sum_{i}^{a}\sum_{k}^{c} y_{ijk}\; j = 1, 2, \ldots, b \tag{11}$$

$$\begin{aligned} SS_{AB} &= \frac{1}{c}\sum_{i}^{a}\sum_{j}^{b} y_{ij.}^{2} - \frac{1}{abc} y_{...}^{2} - SS_{A} - SS_{B};\, y_{ij.} \\ &= \sum_{k}^{c} y_{ijk}\; i = 1, 2, \ldots, a;\, j = 1, 2, \ldots, b \end{aligned} \tag{12}$$

$$SS_{IDV} = SS_{total} - SS_{A} - SS_{B} - SS_{AB} \tag{13}$$

where A, B, and IDV represent the climate models, climate change scenarios, and inter-decadal variability with a, b, and c available choices; y_{ijk} denotes the projection with the choice of i^{th} CMIP6 model, j^{th} climate change scenario, and k^{th} period. The contribution (C_X) of each scheme or the interrelated setting (X) to the total variability can be defined as:

$$C_{X} = \frac{SS_{X}}{SS_{total}} \times 100\% \tag{14}$$

The sum of squares due to inter-decadal variability are assumed to be errors/residuals (SS_{error}). The statistical significance of climate models, climate change scenarios, and their interrelated settings can be determined by F-test assuming that the residuals are normally and independently distributed.

$$F_{IX} = \frac{SS_{IX}/df_{IX}}{SS_{error}/df_{error}} \tag{15}$$

where df_{IX} and df_{error} denote the degree of freedom for contributing factors (IX) and errors, respectively. A contributing factor is considered significant if the calculated p-value is smaller than the predefined significance level (0.05 in this study).

Data availability

Monthly outputs from the latest global reanalysis dataset ERA5 can be obtained from the European Centre for Medium-Range Weather Forecasts (ECMWF, https://www.ecmwf.int/en/forecasts/dataset/ecmwf-reanalysis-v5). The outputs from GCMs are downloaded from the Coupled Modeling Intercomparison Project (CMIP6) data set archive (https://esgf-node.llnl.gov/search/cmip6/). The data for generating the figures in this study are available at https://doi.org/10.5281/zenodo.15543845.

Code availability

The scripts generated during this study are available upon request from the corresponding author.

Received: 12 February 2025; Accepted: 3 June 2025;
Published online: 19 June 2025

References

1. Gernaat, D. E. H. J. et al. Climate change impacts on renewable energy supply. *Nat. Clim. Change* **11**, 119–125 (2021).
2. Lu, T. et al. India's potential for integrating solar and on- and offshore wind power into its energy system. *Nat. Commun.* **11**, 4750 (2020).
3. Dvorak, M. J., Stoutenburg, E. D., Archer, C. L., Kempton, W. & Jacobson, M. Z. Where is the ideal location for a US East Coast offshore grid? *Geophys. Res. Lett*. **39**, L06804 (2012).
4. Gao, Q. et al. Assessment of wind and wave power characteristic and potential for hybrid exploration in Australia. *Renew. Sustain. Energy Rev.* **168**, 112747 (2022).
5. Wen, Y., Kamranzad, B. & Lin, P. Joint exploitation potential of offshore wind and wave energy along the south and southeast coasts of China. *Energy* **249**, 123710 (2022).
6. Musgrove, P. J. Energy analysis of wave-power and wind-power systems. *Nature* **262**, 206–207 (1976).
7. Breivik, Ø., Aarnes, O. J., Abdalla, S., Bidlot, J.-R. & Janssen, P. A. E. M. Wind and wave extremes over the world oceans from very large ensembles. *Geophys. Res. Lett.* **41**, 5122–5131 (2014).
8. Wilkie, D. & Galasso, C. Impact of climate-change scenarios on offshore wind turbine structural performance. *Renew. Sustain. Energy Rev.* **134**, 110323 (2020).
9. Bethel, B. J. Joint Offshore Wind and Wave Energy Resources in the Caribbean Sea. *J. Mar. Sci. Appl.* **20**, 660–669 (2021).
10. Lin, Y.-H. & Fang, M.-C. An Integrated Approach for Site Selection of Offshore Wind-Wave Power Production. *IEEE J. Ocean. Eng.* **37**, 740–755 (2012).
11. Onea, F., Ciortan, S. & Rusu, E. Assessment of the potential for developing combined wind-wave projects in the European nearshore. *Energy Environ* **28**, 580–597 (2017).
12. Lira-Loarca, A., Ferrari, F., Mazzino, A. & Besio, G. Future wind and wave energy resources and exploitability in the Mediterranean Sea by 2100. *Appl. Energy* **302**, 117492 (2021).
13. Ribeiro, A. et al. Assessment of Hybrid Wind-Wave Energy Resource for the NW Coast of Iberian Peninsula in a Climate Change Context. *Appl. Sci.* **10**, 7395 (2020).
14. Ibarra-Berastegui, G., Sáenz, J., Ulazia, A., Sáenz-Aguirre, A. & Esnaola, G. CMIP6 projections for global offshore wind and wave energy production (2015–2100). *Sci. Rep.* **13**, 18046 (2023).
15. Marshall, A. G., Hemer, M. A., Hendon, H. H. & McInnes, K. L. Southern annular mode impacts on global ocean surface waves. *Ocean Model* **129**, 58–74 (2018).
16. Lee, D. Y., Petersen, M. R. & Lin, W. The Southern Annular Mode and Southern Ocean Surface Westerly Winds in E3SM. *Earth Space Sci* **6**, 2624–2643 (2019).
17. Rosenblatt, M. Remarks on Some Nonparametric Estimates of a Density Function. *Ann. Math. Stat.* **27**, 832–837 (1956).
18. Eyring, V. et al. Overview of the Coupled Model Intercomparison Project Phase 6 (CMIP6) experimental design and organization. *Geosci. Model Dev.* **9**, 1937–1958 (2016).
19. Hersbach, H. et al. The ERA5 global reanalysis. *Q. J. R. Meteorol. Soc.* **146**, 1999–2049 (2020).
20. Tian, C. et al. Northward Shifts of the Sahara Desert in Response to Twenty-First-Century Climate Change. *J. Clim.* **36**, 3417–3435 (2023).
21. Song, T., Huang, G. & Wang, X. Neglected Spatiotemporal Variations of Model Biases in Ensemble-Based Climate Projections. *Geophys. Res. Lett.* **49**, e2022GL098063 (2022).
22. Raftery, A. E. Bayesian Model Selection in Social Research. *Sociol. Methodol.* **25**, 111–163 (1995).
23. Raftery, A. E., Gneiting, T., Balabdaoui, F. & Polakowski, M. Using Bayesian Model Averaging to Calibrate Forecast Ensembles. *Mon. Weather Rev.* **133**, 1155–1174 (2005).
24. Duan, Q., Ajami, N. K., Gao, X. & Sorooshian, S. Multi-model ensemble hydrologic prediction using Bayesian model averaging. *Adv. Water Resour.* **30**, 1371–1386 (2007).
25. Box, G. E. P. & Cox, D. R. An Analysis of Transformations. *J. R. Stat. Soc. Ser. B Methodol.* **26**, 211–252 (1964).
26. Dempster, A. P., Laird, N. M. & Rubin, D. B. Maximum Likelihood from Incomplete Data Via the EM Algorithm. *J. R. Stat. Soc. Ser. B Methodol.* **39**, 1–22 (1977).
27. Bishop, C. T. & Donelan, M. A. Chapter 4 Wave Prediction Models. in *Elsevier Oceanography Series* (eds. Lakhan, V. C. & Trenhaile, A. S.) vol. 49 75–105 (Elsevier, 1989).
28. Dean, R. G. & Dalrymple, R. A. *Water Wave Mechanics for Engineers and Scientists* 2 (World Scientific, Singapore, 1991).
29. Llovel, W., Balem, K., Tajouri, S. & Hochet, A. Cause of Substantial Global Mean Sea Level Rise Over 2014–2016. *Geophys. Res. Lett.* **50**, e2023GL104709 (2023).
30. Lei, Y. et al. Co-benefits of carbon neutrality in enhancing and stabilizing solar and wind energy. *Nat. Clim. Change* **13**, 693–700 (2023).
31. Song, T., Huang, G., Wang, X. & Zhou, X. Factorial Sensitivity Analysis of Physical Schemes and Their Interactions in RegCM. *J. Geophys. Res. Atmospheres* **125**, e2020JD032501 (2020).

Acknowledgements

This research was supported by the Natural Science Foundation (52221003), the National Key R&D Program of China (2023YFC3206503), the Natural Science Foundation (52279002, 52279003, U2040212), MWR/CAS Institute of Hydroecology, and Natural Science and Engineering Research Council of Canada.

Author contributions

X.Z. and G.H. conceived the study. X.Z. performed the data analysis. X.Z. and C.L. led the writing of this study, with discussion and improvement from Y.L., C.T., T.S., X.Z., W.T and B.P.

Competing interests

The authors declare no competing interests.

Additional information

Supplementary information The online version contains supplementary material available at https://doi.org/10.1038/s43247-025-02437-4.

Correspondence and requests for materials should be addressed to Guohe Huang.

Peer review information *Communications Earth & Environment* thanks Stefano Susini and the other, anonymous, reviewer(s) for their contribution to the peer review of this work. Primary Handling Editors: I-Yun Hsieh and Aliénor Lavergne. A peer review file is available